

# Tracking the role of compressive strain in bowl-Like Co-MOFs structural evolution in water oxidation reaction

Meihuan Liu<sup>a,1</sup>, Shuowen Bo<sup>b,c,1</sup>, Jing Zhang<sup>c,1</sup>, Qinghua Liu<sup>c,\*</sup>, Jun Pan<sup>a,\*</sup>, Hui Su<sup>b,\*</sup>

<sup>a</sup> State Key Laboratory for Powder Metallurgy, Central South University, Changsha, Hunan 410083, China

<sup>b</sup> Key Laboratory of Light Energy Conversion Materials of Hunan Province College, College of Chemistry and Chemical Engineering, Hunan Normal University, Changsha, Hunan 410081, China

<sup>c</sup> National Synchrotron Radiation Laboratory, University of Science and Technology of China, Hefei, Anhui 230029, China

## ARTICLE INFO

### Keywords:

Water oxidation  
Compression strain  
Bowl-like MOFs  
*In situ* characterization  
Structural evolution

## ABSTRACT

Dynamic structural evolution of catalyst active sites is crucial to for transition metal-catalyzed oxygen evolution reaction (OER). Yet, the elucidation of their mechanism behind the compressive-strain-induced reconstruction during OER process remains enigmatic. Here, we construct a bowl-like cobalt-based metal-organic frameworks (BL-Co-MOFs) catalyst with compressive strain to investigate the effect of strain on the structural evolution process and the OER mechanism. *In situ* techniques directly observe that compressive strain exists in the reconstruction of the potential-driven CoOOH-like active phase with contractile interatomic Co—Co distance, promoting a direct O—O radical coupling over the Co sites (Co—O—O—Co) during the OER process. This disrupts the constrains of the inherent linear scaling relationship and achieves the kinetic-faster oxide path mechanism (OPM) during OER process. Consequently, the BL-Co-MOFs exhibit a huge mass activity of  $12516 \text{ A g}_{\text{metal}}^{-1}$  and a large turnover frequency of  $6888 \text{ h}^{-1}$  at a low overpotential of 275 mV ( $300 \text{ mA cm}^{-2}$ ).

## 1. Introduction

The oxygen evolution reaction (OER), an important half-reaction of water splitting and rechargeable metal-air batteries, plays an impressive role in sustainable energy conversion and storage[1–3]. Subject to four proton-electron transfers, intricate reaction pathways, and the inherent linear scaling relation (LSR) between multiple intermediate species (\*OH, \*O and \*OOH), the OER suffers from sluggish kinetics and large overpotentials[4–6]. Among them, the NiFe-oxides and -oxyhydroxides have emerged as exceptional OER electrocatalysts[7–9]. However, they follow the conventional adsorbate evolution mechanism (AEM), which makes it difficult to independently regulate the adsorption energy of multiple intermediates[10,11]. This results in a large overpotential ( $>300 \text{ mV}$  at  $10 \text{ mA cm}^{-2}$ ). Recently, some efforts have been made to regulate the covalency of metals and oxygen so that they follow the lattice-oxygen-mediated mechanism (LOM), thereby enhancing catalytic activity[12–14]. Unfortunately, the generation of excessive oxygen vacancy in LOM easily results in the dissolution of the surface-active phase of catalyst, and thus it is hard to achieve stable activity under a large current density[15,16]. Generally, hydroxyl species attack the

active sites of the metal oxo moiety, and radical coupling between two metal oxo moieties is considered to be the key for reaction pathways and mechanisms, but it is difficult to directly detect these species in a real reaction[17,18]. Therefore, identifying the structure of the catalytically active sites and unveiling the OER mechanisms under the reaction conditions is highly desirable to offer guidelines for designing targeted electrocatalysts.

Recently, essential progress in the development of advanced electrocatalysts for OER technology has been made, such as nanostructured transition metal electrocatalysts, high entropy materials, and COF-based catalysts[19–23]. Actually, the good performance of transition metal oxides in the OER process is probably derived from the presence of a surface-reconstructed oxyhydroxide phase ( $\text{MO}_x\text{OH}_y$ )[24,25]. More interestingly, the reconstructed surface-active phase displays superior OER performances and stability than the as-synthesized bulk oxy-/hydroxides material, owing to the accessibility of active sites and active electronic state[26,27]. Nevertheless, achieving a thorough comprehension of the reaction mechanism remains a significant challenge, given the intricacy of the reconstructed surface-structure. Previous studies have demonstrated that ion doping, stress engineering and

\* Corresponding authors.

E-mail addresses: [qhliu@ustc.edu.cn](mailto:qhliu@ustc.edu.cn) (Q. Liu), [jun.pan@csu.edu.cn](mailto:jun.pan@csu.edu.cn) (J. Pan), [suhui@hunnu.edu.cn](mailto:suhui@hunnu.edu.cn) (H. Su).

<sup>1</sup> These authors contributed equally: Meihuan Liu, Shuowen Bo, Jing Zhang.

morphology design can modulate the electronic properties of reconstructed structures, thereby influencing the adsorption of intermediate species and OER performance[28–30]. Furthermore, constructing a localized metal pair with a contractive distance enables the oxide path mechanism (OPM) in the OER process, which can break the LSR to bypass  $^*OOH$  production and then enhance catalytic activity[31,32]. For purpose, compressive strain is introduced in Co-based metal-organic frameworks (Co-MOFs) for modulating the reconstructed active phase with contractile dual-atom sites, which enables direct coupling of O–O bonds. More importantly, a deeper understanding of the structural evolution of active sites incuced by strain under the working condition may yield valuable new insights into the reaction pathway and mechanism.

Here, to satisfy the OPM design rule, we develop compressive-strain bowl-like Co-MOFs (BL-Co-MOFs) as highly active OER electrocatalysts prepared by a facile and controllable morphology-regulation to induce compressive strain. The introduction of compressive strain expedites the production of reconstructed oxyhydroxide phase and reduces spacing of Co sites, and hence the OPM is realized in compressive-strain BL-Co-MOFs. At the atomic level, *in situ* X-ray absorption fine structure (XAFS) spectroscopy reveals that the interatomic Co–Co distance in the potential-driven CoOOH-like active phase (2.72 Å) is shorter than that of prototype CoOOH (2.92 Å). Especially, this structural self-rearrangement can facilitate direct O–O radical coupling (Co–O–O–Co), successfully bypassing  $^*OOH$  species generation, as validated by *in situ* synchrotron radiation infrared spectroscopy (SRIR) and *in situ* Raman results, and subsequently achieving a kinetically faster OPM during OER process. The well-designed BL-Co-MOFs deliver low overpotentials of 259 and 275 mV to achieve current densities of 100 and 300 mA cm<sup>−2</sup>, respectively, and sustain operation at large current density over an extended period of 80 h. Most significantly, a high mass activity of 12516 A g<sub>metal</sub><sup>−1</sup> and a large TOF of 6888 h<sup>−1</sup> are observed for BL-Co-MOFs, ~1526 and 675 times greater than those of commercial RuO<sub>2</sub> (8.2 A g<sup>−1</sup> and 10.2 h<sup>−1</sup>, respectively).

## 2. Experimental section

### 2.1. Synthesis of BL-Co-MOFs

In order to weak the rigidity of MOF structure for constructing open-mouthed structure (bowl-like), the polyoxometalates (such as hexaammonium molybdate) was introduced into synthetic systems. The polyoxometalates anions would compete with organic ligands to coordinate with the metal clusters, thus partially substitute the organic ligands and break the infinite structure towards a novel bowl-like structure. Typically, 1 mL Co(acac)<sub>3</sub> (9 mg mL<sup>−1</sup>, DMF), 0.25 mL H<sub>3</sub>BTC (60 mg mL<sup>−1</sup>, DMF), 0.5 mL PVP (40 mg mL<sup>−1</sup>, DMF), 1 mL hexamethylenetetramine (20 mg mL<sup>−1</sup>, EtOH), 0.25 mL thioacetamide (20 mg mL<sup>−1</sup>, DMF) and 0.06 mL (NH<sub>4</sub>)<sub>6</sub>Mo<sub>7</sub>O<sub>24</sub>·4 H<sub>2</sub>O (150 mg mL<sup>−1</sup>, H<sub>2</sub>O) were added in 5 mL DMF to form a homogeneous solution. In a 50 mL Teflon-lined stainless-steel autoclave, the temperature was raised to 180 °C rapidly from room temperature and then kept for 12 h in an oven. After the solution was cooled down naturally to room temperature, the precipitate product was washed by EtOH for several times.

### 2.2. Synthesis of Co-MOFs

The morphology and structure can be precisely regulated by the hydrothermal reaction time. The Co-MOFs sample was prepared following the same procedure of BL-Co-MOFs but shorten the reaction time to 20 min.

### 2.3. Electrochemical measurements

All electrochemical measurements were performed in a standard three-electrode electrochemical cell by CHI760E electrochemical

workstation (CH Instruments, Inc., Austin, TX), where the prepared electrodes immersed in a KOH electrolyte solution (1 M). 1 × 1 cm<sup>2</sup> carbon cloth (CC) with catalyst, carbon rod and the Hg/HgO electrode act as the working, counter and reference electrode, respectively. All final potentials were converted to reversible hydrogen electrode (RHE). The mass loading of catalyst on the electrode was 1 mg cm<sup>−2</sup>. Linear sweep voltammetry (LSV) curves were measured at a rate of 1 mV s<sup>−1</sup> with 90 % iR compensation after several cyclic voltammetry tests until stable. Tafel slopes were calculated by plotting potential  $\eta$  against log  $|j|$  from LSV curves. For OER tests, the electrochemical double-layer capacitance ( $C_{dl}$ ) was calculated by cyclic voltammetry curves with scanning rates of 20, 40, 60, 80, and 100 mV s<sup>−1</sup>. The ECSA values were calculated from the measured double layer capacitance divided by the specific capacitance of the sample:  $ECSA = C_{dl} / C_s$ . The roughness factor (RF) was calculated by taking the estimated ECSA and  $S_{geo}$ :  $RF = ECSA / S_{geo}$ , and the definition of specific activity refers to the specific current density  $J_{ECSA}$ , which was calculated according to  $J_{ECSA} = J / RF$ .

### 2.4. In situ XAFS measurements

The Co K-edge XAFS data was collected at the 1W1B station in Beijing Synchrotron Radiation Facility (BSRF, China). The storage ring of BSRF was operated at 2.5 GeV with a maximum current of 250 mA. Electrochemical *in-situ* XAFS measurements were carried out by a homemade cell in a 1 M KOH electrolyte. The XAFS spectra were collected through fluorescence mode with a 19-element solid-state detector. The BL-Co-MOFs electrocatalyst was cut into 1 × 2 cm<sup>2</sup> pieces and then sealed in a cell by Kapton film. To obtain the evolution information of the active sites during the electrochemical reaction, a series of representative potentials (1.15–1.40 V) were applied to the electrode. During the collection of XAFS measurements, position of the absorption edge ( $E_0$ ) was calibrated using a standard sample of Co. Quantitative curve fittings were carried out for the Fourier transformed  $k^3\chi(k)$  in R-space using the ARTEMIS module of IFEFFIT. The amplitude  $F_i(k, R_i)$  and phase shifts  $\Phi_i(k, R_i)$  functions for the first-shell of Co–O and the second-shell of Co–Co coordination were calculated with the FEFF8 in the muffin-tin (MT) self-consistent-field approximation. Default values of MT radii and muffin-tin radii overlap of 15 % between contiguous spheres were used to simulate the atomic bond. To account for energy dependent exchange-correlation potential, the energy- and position-dependent optical Hedin-Lundqvist potential was employed. Considering the potential-driven CoOOH-like phase during OER process, the calculations were performed for a cluster with radius of 8 Å having the structure of cobalt oxyhydroxide and centered at the Co–O (Co–Co) atom, respectively.

### 2.5. In situ Raman measurements

*In situ* Raman measurements were collected at Laser Confocal Raman Microscope (LabRAM HR Evolution) through a homemade top-plate cell. To avoid signal differences caused by sample shedding, Raman spectra were collected after a constant potential was applied to the catalyst electrode for 5 min. Before each systemic OER measurement, the background spectrum of the catalyst electrode was acquired under potential free condition (Ex-situ), and then the measured potential ranges were 1.00–1.50 V vs. RHE.

## 3. Results and discussion

### 3.1. Structure characterizations of BL-Co-MOFs

The bowl-like Co-MOFs (BL-Co-MOFs) with compressive strain was prepared through a controllable hydrothermal method (see more details in the Methods section). In order to weak the rigidity of MOF structure for constructing open-mouthed structure (bowl-like), the polyoxometalates (such as hexaammonium molybdate) was introduced into

synthetic systems. The polyoxometalates anions would compete with organic ligands to coordinate with the metal clusters, thus partially substitute the organic ligands and break the infinite structure towards a novel bowl-like structure[33–35]. Meanwhile, the morphology and structure can be precisely regulated by the hydrothermal reaction time. The as-synthesized samples were verified by scanning electron microscopy (SEM) and transmission electron microscopy (TEM). When the reaction time was controlled in 20 min, the SEM and TEM images in Figs. 1a, 1b and Figure S1 show that the Co-MOFs sample primarily comprised solid spheres with a diameter of 200–300 nm, without the observation of bowl-like structures. However, a small amount of surface collapse occurs, attributed to the gradual dissolution of the inner core resulting from the thermodynamic instability of the rapidly formed Co-MOF nanosphere and imbalanced diffusion between outward and inward ions. Upon prolonging the reaction time to 12 h, the SEM image (Fig. 1c) clearly displays that the uniform BL-Co-MOFs possess hollow cavities with a diameter of approximately 200 nm. The uniform bowl-like structures were further confirmed by TEM image (Fig. 1d). Therefore, when the reaction time is extended, the inner core dissolves gradually resulting from thermodynamic instability of the fast formed Co-MOF nanosphere and unbalanced diffusion between outward and inward ions, leading to the formation of the concave-surface bowl-like structure. This bowl-like structure introduces compressive strain in the BL-Co-MOFs. The  $N_2$  physisorption isotherms reveal a slightly higher specific surface area of BL-Co-MOFs in comparison with Co-MOFs (Figure S2), which reveals large open active sites and accessible reactive species.

Meanwhile, the bowl-like structure may induce compressive strain in

the sample, a phenomenon ascertainable through the X-ray diffraction (XRD) pattern. The low crystallinity of BL-Co-MOFs may be attributed to polyoxometalates anions competing with organic ligands and breaking the infinite structure. The XRD pattern in Fig. 1e of these two MOFs shows a broad peak assigned to (2, -1, 0), which is consistent with the reported M-BTC MOFs[36], while the peak located at about  $34^\circ$  may be attributed to the  $MoS_2$  (1, 0, 0) plane[37]. The absence of some peaks in the  $2\theta$  values of Co-MOFs and BL-Co-MOFs compared to the simulated M-BTC might be ascribed to the competitive coordination of polyoxometalates. Due to the introducing of Mo and S source from molybdate and thioacetamide, respectively, the  $MoS_2$  can be easily generated under hydrothermal reaction condition. The participation of molybdate and thioacetamide could weaken the rigidity of MOF structure for constructing bowl-like structure (Figures S3–5). The bowl-like morphology depends on the amount of molybdate and thioacetamide as well as the reaction time. Notably, the peak in BL-Co-MOFs slightly shifts toward higher angles compared to Co-MOFs, suggesting the occurrence of compressive strain after the formation of the bowl-like structure in BL-Co-MOFs[38]. Moreover, as depicted in the high-resolution TEM images in Fig. 1f and Figures S6–8, the lattice fringe parameters of the BL-Co-MOFs were measured at 2.64 Å, corresponding to  $MoS_2$  (100) planes, which is conspicuously smaller than that of the Co-MOFs (2.72 Å) (Figure S7). This discrepancy represents the compressive strain generated on the BL-Co-MOFs due to the formed bowl-like structure. The corresponding elemental mapping spectra and line-scanning spectra of BL-Co-MOFs (Fig. 1g and Figures S9, S10) demonstrated that C, S, N, Co, Mo, and O are distributed well throughout the entire bowl-like structures. In addition, the relative mass ratios of Co

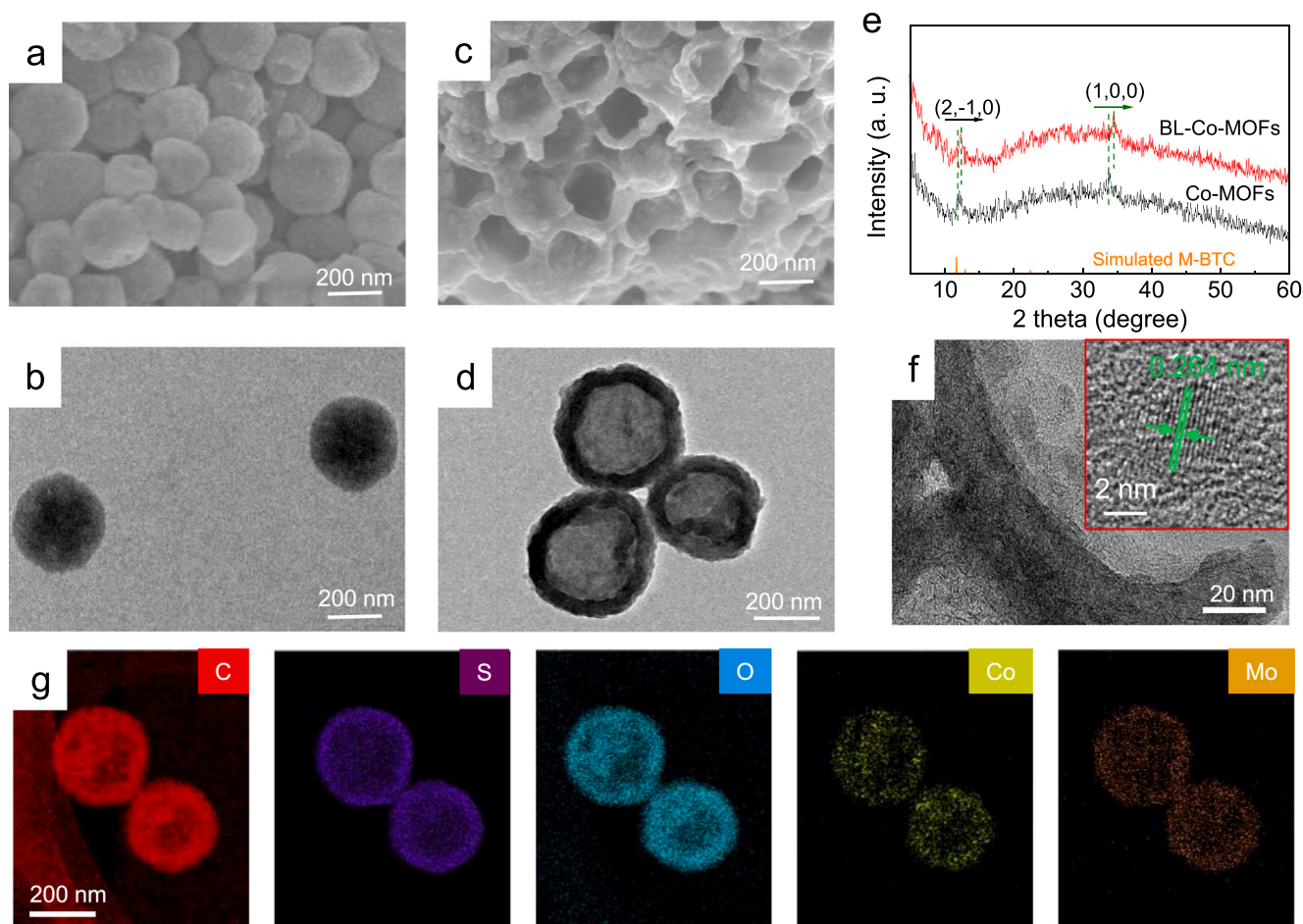


**Fig. 1.** (a) SEM and (b) TEM images for Co-MOFs. (c) SEM and (d) TEM images for BL-Co-MOFs. (e) XRD pattern of Co-MOFs, BL-Co-MOFs and simulated M-BTC MOF (CCDC No. 636900, hexagonal, P63/mcm). (f) HRTEM image and (g) EDS mapping images for BL-Co-MOFs.

and Mo in BL-Co-MOFs and Co-MOFs are analyzed (Table S1, S2 and Figure S11). As the reaction time extended from 20 min to 12 h, the sphere like Co-MOFs transformed into a bowl-like structure (BL-Co-MOFs), instigating the compressive strain of this catalyst. Above all, the HRTEM images and XRD patterns clearly demonstrate the compression strain generated in the BL-Co-MOFs is owing to the bowl-like structure.

To investigate the surface electronic structures and chemical states of the Co sites in BL-Co-MOFs, the soft X-ray absorption spectroscopy (XAS) of Co *L*-edge (Fig. 2a) was performed [39,40]. The Co *L*<sub>3</sub>-edge XAS spectra of BL-Co-MOFs exhibit distinctive doublets features (labelled as A and B), but only one dominant peak (labelled as A) is observed for the Co-MOFs. The obvious peak B in BL-Co-MOFs reveals the reduced electron occupancy in the outer 3d orbital of Co [41]. The higher oxidation state for BL-Co-MOFs is further confirmed by the Co 2p XPS results in Fig. 2b [42], suggesting that more electrons are transferred from Co to nearby atoms after the introduction of compressive strain [35]. The low-energy shift for Co–O of O 1s XPS in BL-Co-MOFs verifies the electron transfer from Co to adjacent O, which matches the Co 2p XPS results (Figure S14). Additionally, X-ray absorption near-edge spectra (XANES) of the Co *K*-edge in Fig. 2c reveals a middle valence state Co (+2). The higher energy position of absorption pre-edge in BL-Co-MOFs relative to Co-MOFs signifies a higher valence state of the Co sites. The alterations in the oxidation state consequent to the introduction of the bowl-like structure can be revealed by the first derivative of the Co *K*-edge XANES spectra in Fig. 2d. It displays that a larger energy position of first derivative maximum is observed for BL-Co-MOFs in comparison with that of Co-MOFs, suggesting a higher Co oxidation state in BL-Co-MOFs. Furthermore, the fitted average oxidation states in Fig. 2e distinctly delineate the valence state of Co as +1.96 and +2.26 for Co-MOFs and BL-Co-MOFs, respectively, signifying a discernible transfer of electrons from Co to adjacent O. To further determine the local coordination environment of Co sites in the samples, the extended XAFS (EXAFS) spectra were plotted in Fig. 2f. In the Fourier-transform (FT) curves of the Co *K*-edge EXAFS spectra, the main peaks in the

1.5–1.6 Å range can be assigned to the first shell of the Co–O coordination [43]. To further quantify the local coordination structure of Co, the EXAFS curves of Co atom were fitted (Figure S15 and Table S3). The first-shell of Co–O bond in BL-Co-MOFs is 2.01 Å, which is shorter than the Co–O bond (2.08 Å) in Co-MOFs, suggesting the compressive strain generated on the BL-Co-MOFs due to formation of bowl-like structure. Thus, these results reveal that the shortened Co–O bonds in BL-Co-MOFs may effectively reduce the electron occupancy in the outer 3d orbital of Co sites in the samples.

### 3.2. The OER performances of BL-Co-MOFs

To evaluate the electrocatalytic OER activity of BL-Co-MOFs, electrochemical measurements were carried out in a three-electrode system using 1 M KOH as the electrolyte, with Co-MOFs and RuO<sub>2</sub> serving as comparative references. From the linear sweep voltammetry (LSV) curves shown in Fig. 3a, only a small overpotential of 259 mV is required for BL-Co-MOFs to achieve a current density of 100 mA cm<sup>−2</sup>, substantially outperforming that of both Co-MOFs (390 mV) and RuO<sub>2</sub> (433 mV), endowing BL-Co-MOFs as one of the best non-noble OER electrocatalysts (Table S4). In Fig. 3b, BL-Co-MOFs just need 275 mV to deliver high current densities of 300 mA cm<sup>−2</sup>, far beyond those of the counterpart samples. As illustrated in Fig. 3c, the Tafel slope of the BL-Co-MOFs is only 61.6 mV dec<sup>−1</sup>, superior to that of Co-MOFs (74.2 mV dec<sup>−1</sup>) and RuO<sub>2</sub> (106.6 mV dec<sup>−1</sup>). Furthermore, according to electrochemical impedance spectroscopy analysis (Figure S16), BL-Co-MOFs presents lower charge-transfer resistance. This indicates that the OER kinetics are promoted and electron transfer are enhanced for BL-Co-MOFs, likely due to the greater number of accessible active sites and high mass transfer rate realized in bowl-like structures. To further identify the electrochemically active surface area (ECSA) of BL-Co-MOFs, the electrochemical double-layer capacitance (*C*<sub>dl</sub>) was calculated (Figure S17) [44]. The BL-Co-MOFs displays the highest *C*<sub>dl</sub> (11.6 mF cm<sup>−2</sup>) among the other reference samples, indicating a greater

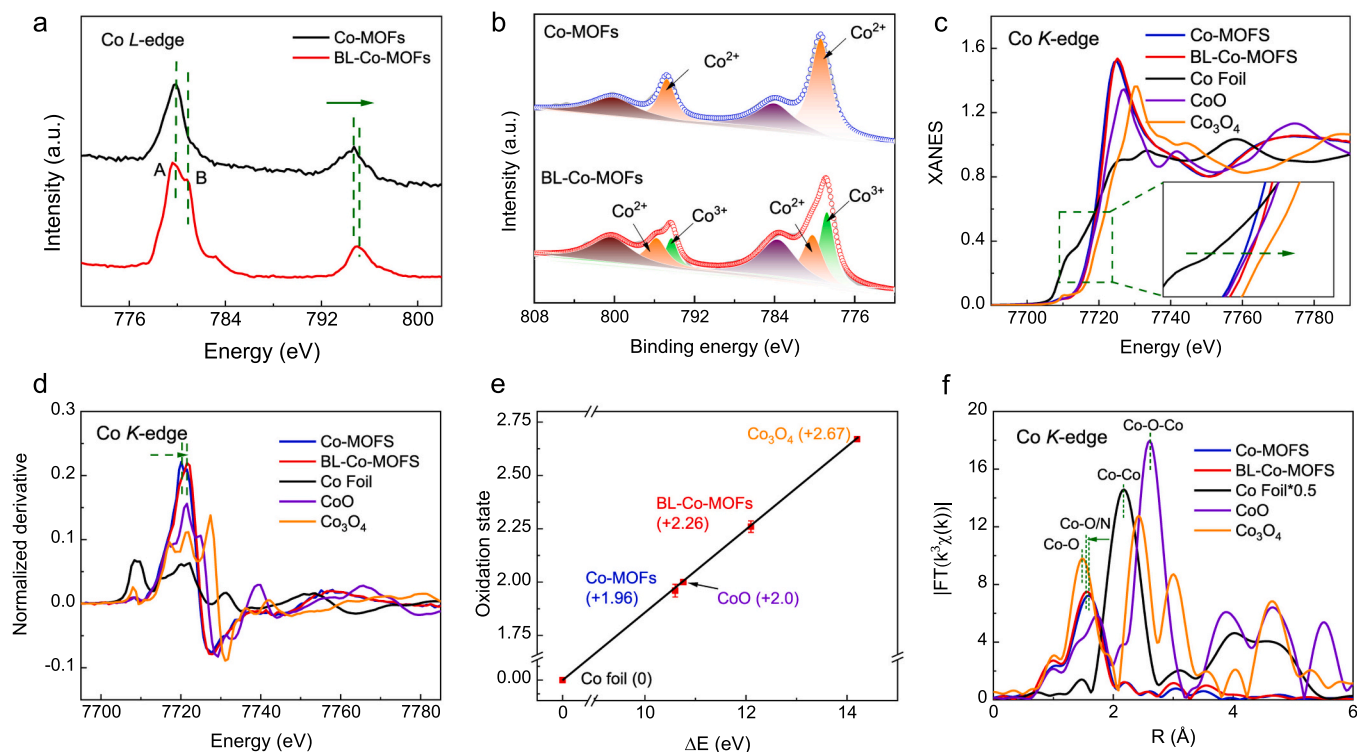


**Fig. 2.** (a) Co *L*-edge XAS spectra and (b) high resolution Co 2p XPS spectra images for Co-MOFs and BL-Co-MOFs. (c) Co *K*-edge XANES spectra (the inset expresses the partially enlarged data). (d) First derivative of the Co *K*-edge XANES spectra. (e) Fitted average oxidation state of Co from XANES spectra. (f) Corresponding EXAFS spectra of Co-MOFs, BL-Co-MOFs and other reference samples.

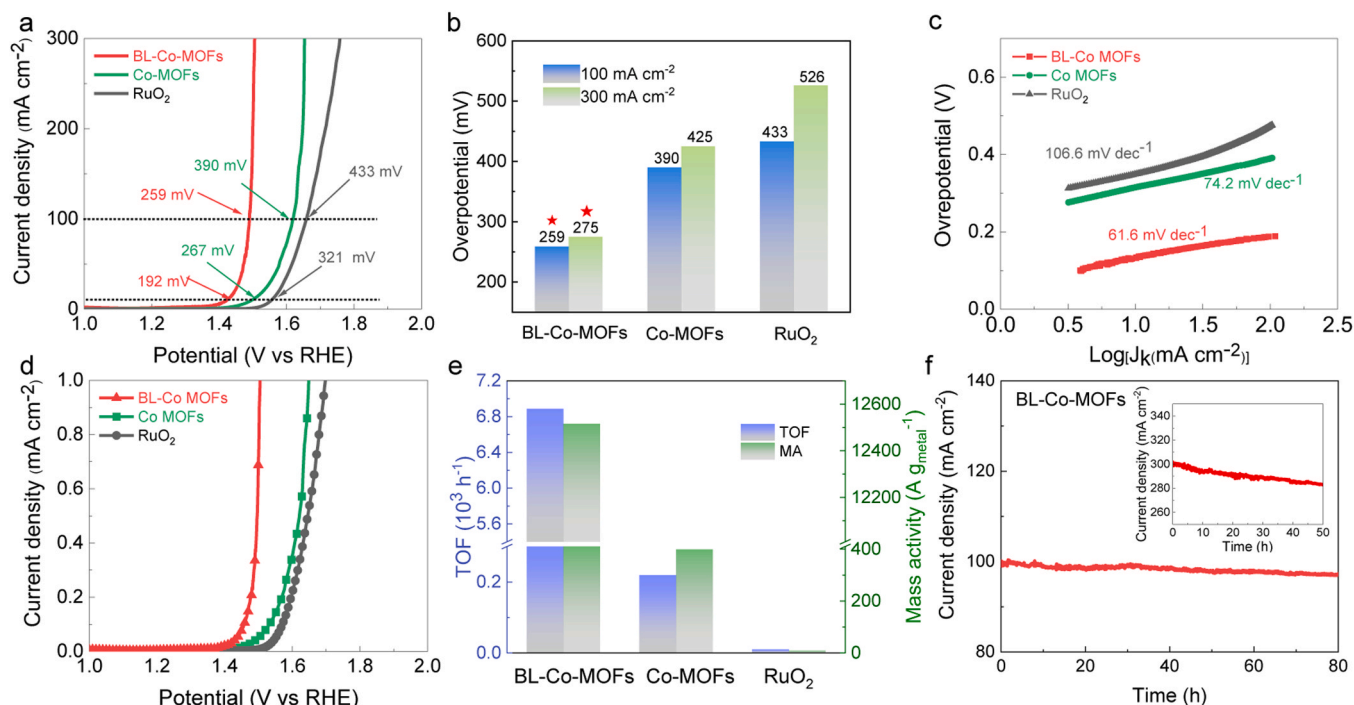


**Fig. 3.** (a) LSV curves of BL-Co-MOFs, Co-MOFs, and RuO<sub>2</sub>. (b) Comparison of the overpotentials at current densities of 100 and 300 mA cm<sup>-2</sup> between the catalysts and RuO<sub>2</sub>. (c) Tafel slope. (d) Polarization curves based on the ECSA. (e) MA and TOF of BL-Co-MOFs, Co-MOFs, and RuO<sub>2</sub>. (f) Stability curves of BL-Co-MOFs and RuO<sub>2</sub>. All the measurements were performed in 1 M KOH.

abundance of the active sites in the BL-Co-MOFs. As expected, the BL-Co-MOFs demonstrates the best specific activity when the current density was normalized per ECSA (Fig. 3d).

To assess the intrinsic activity of the BL-Co-MOFs, the mass activity

(MA) and turnover frequency (TOF) were evaluated in Fig. 3e and Table S5. Notably, BL-Co-MOFs shows a large mass activity of 12516 A g<sub>metal</sub><sup>-1</sup> and an ultrahigh TOF of 6888 h<sup>-1</sup> under a typical overpotential of 275 mV, ~1526 and 675 times higher than those of the commercial

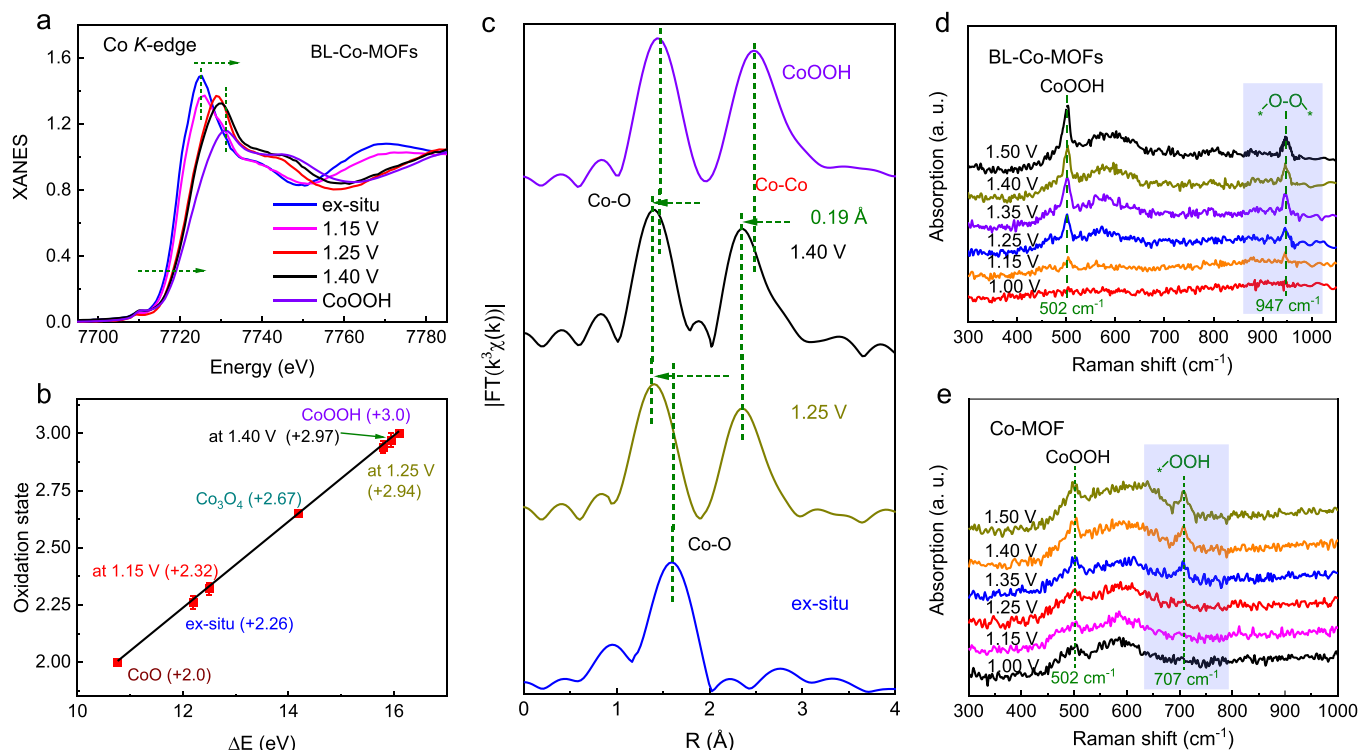


**Fig. 4.** (a) *In situ* Co K-edge XANES spectra of BL-Co-MOFs at different applied potential during the OER test. (b) The fitted average oxidation state of Co from XANES spectra. (c) Corresponding EXAFS spectra of BL-Co-MOFs at different applied potentials and reference CoOOH. *In situ* Raman spectra in the range of 300–1000 cm<sup>-1</sup> of (d) BL-Co-MOFs and (e) Co-MOFs.

$\text{RuO}_2$  ( $8.2 \text{ A g}^{-1}$  and  $10.2 \text{ h}^{-1}$ , respectively). More importantly, the chronoamperometry curve of BL-Co-MOFs shows only a slight decay of about 3 % of the initial current density was experienced after an 80-hour OER test at a high current density of  $100 \text{ mA cm}^{-2}$  (Fig. 3f and Figure S18), suggesting robust long-term stability of the catalyst. A higher current density of  $300 \text{ mA cm}^{-2}$  was also tested, and the BL-Co-MOFs still maintains  $\sim 93.4$  % of the initial current density after 50 h operation. The characterization results of the samples before and after OER operation were depicted in Figures S19 and S20. The bowl-like structure of BL-Co-MOFs was retained and an obvious surface reconstruction was observed after the long-term OER operation, which confirms good structural robustness and excellent oxygen electrocatalytic durability of the BL-Co-MOFs.

### 3.3. In situ XAFS and Raman spectroscopy of BL-Co-MOFs

To promptly elucidate the catalytic mechanism of compression-strain BL-Co-MOFs during the OER process, *in situ* XAFS measurements were performed[45]. As depicted in the Co *K*-edge XANES spectra of BL-Co-MOFs (Fig. 4a). The absorption edge position shifts toward higher energy side when the applied voltage increased, ultimately approaching the location of  $\text{CoOOH}$ . The increased oxidation state of Co sites can be further confirmed by the energy position of the first derivative maximum from XANES spectra (Figure S21). To further quantify the change in oxidation state of Co sites, the average valence state was fitted on the basis of Co *K*-edge XANES in Fig. 4b. The average metal valence state increases from  $+2.32$  to  $+2.94$  in BL-Co-MOFs with potentials increasing from 1.15 to 1.25 V, indicating a rapid pre-oxidation process. Interestingly, in Fig. 4c, when the potentials increase to 1.25 V, new peaks located at  $\sim 1.40$  and  $2.35 \text{ \AA}$  can be assigned to first-shell of Co—O and second-shell of Co—Co coordination, which means that the low applied potentials can promote the formation of a  $\text{CoOOH}$ -like active phase on the surface of catalyst during OER process. Meanwhile, the increased valence of Co and the unchanged valence of Mo after reaction (Figure S22) indicate that the active site of the reaction is the dynamically-evolved  $\text{CoOOH}$ -like layer. Notably, the apparent bond length of Co—Co in the dynamically-evolved  $\text{CoOOH}$ -like phase is slightly shorter ( $0.19 \text{ \AA}$ ) than that of standard  $\text{CoOOH}$ . It directly proves that the Co—Co distance shortens due to the existence of compressive strain in the dynamically-evolved  $\text{CoOOH}$ -like phase, which provides the structural basis for direct O—O coupling. The intensity of the peak increased slightly with potentials increasing from 1.25 to 1.40 V, indicating that oxygen-containing intermediates were adsorbed at the Co site and excluding the lattice oxygen involved in the reaction (Figure S23). Precisely, the fitted curves of the  $k^3$ -weighted Co *K*-edge EXAFS spectra in Figures S24, S25 and Table S6, show that the Co—Co bond length is  $2.72 \text{ \AA}$  in potential-driven  $\text{CoOOH}$ -like active phase, is shorter than that of prototype  $\text{CoOOH}$  ( $2.92 \text{ \AA}$ ). This indicates the two adjacent Co sites of the dynamically-transformed  $\text{CoOOH}$ -like phase active layer have suitable interatomic spacing attributed to compression strain induced by the bowl-like structure. Importantly, the contracted lattice and shortened Co—Co bond length in the dynamically-evolved  $\text{CoOOH}$ -like phase for BL-Co-MOFs after OER indicate that compressive stress still exists on the surface of the material, which is conducive to direct  $^*\text{O}-\text{O}^*$  radical coupling over a Co dual-atom pair without producing  $^*\text{OOH}$  intermediates for a fast OPM process during OER (Figures S26 and S27).

Furthermore, *in situ* Raman spectroscopy for Co-MOFs and BL-Co-MOFs under increasing potentials were also characterized (Fig. 4d and 4e). A new Raman band at  $500 \text{ cm}^{-1}$  appears at 1.15 V and 1.25 V for BL-Co-MOFs and Co-MOFs, implying the generation of  $\text{CoOOH}$  species at the surface[46]. Interestingly, a new potential-related Raman band at  $947 \text{ cm}^{-1}$  is observed for BL-Co-MOFs when the potentials surpass 1.25 V, which could be attributed to the appearance of  $^*\text{O}-\text{O}^*$  species bridged over Co sites (Co—O—O—Co)[47,48]. In contrast, another Raman peak at  $707 \text{ cm}^{-1}$  emerged for the Co-MOFs is assigned to  $^*\text{OOH}$

species, suggesting a traditional OER mechanism path[49,50]. To further reveal the reaction path during the OER process, the potential-dependent Raman signals for BL-Co-MOFs and Co-MOFs were presented in Figure S28. As the applied potential increases, the amplitude of the peaks in BL-Co-MOFs enhances much more than that of Co-MOFs. The above results reveal that the formed compressive strain in BL-Co-MOFs could accelerate the production of the active oxyhydroxide-like phase with contractive Co—Co distance, resulting in direct O—O coupling over Co sites, which may subsequently promote the OER to follow the OPM mechanism in principle.

### 3.4. In situ SRIR spectroscopy of BL-Co-MOFs

To effectively elucidate the underlying catalytic mechanism during OER process, we further conducted *in situ* SRIR measurements that is sensitive to oxygen-containing species[51]. Accordingly, there are no obvious absorption bands for BL-Co-MOFs in the range  $800\text{--}1400 \text{ cm}^{-1}$  when the applied potential is under 1.15 V (Fig. 5a). With increasing potential to 1.25 V, a new absorption band at a vibration frequency of  $1115 \text{ cm}^{-1}$  is observed, which could be assigned to the key  $^*\text{O}-\text{O}^*$  intermediates over the dual-metal-atom sites because the oxygen species (O—O) stretching vibration is usually in the range  $1100\text{--}1150 \text{ cm}^{-1}$ [52]. This suggests that the key intermediates  $^*\text{O}-\text{O}^*$  produced over the Co sites in the form of Co—O—O—Co structure during the OER. This combination of previous *in situ* XAFS and Raman results clearly reveal that compression strain in bowl-like structure and enhanced potential facilitate the generation of active  $\text{CoOOH}$ -like phase with contracted Co—Co bond, promoting direct O—O radical coupling over the Co sites. For comparison, *in situ* SRIR characterizations were measured under the same conditions for Co-MOFs (Fig. 5b). The absorption band appears at  $1042 \text{ cm}^{-1}$  with the increasing applied potential and shows a potential-dependent relationship. Based on the IR vibration signals of the cobalt and oxygen stretching modes, the band at  $1042 \text{ cm}^{-1}$  can be attributed to the emergency of  $^*\text{OOH}$  intermediates species, suggesting a traditional AEM mechanism[53,54]. Meanwhile, the vibration peak intensities of  $^*\text{O}-\text{O}^*$  ( $1114 \text{ cm}^{-1}$ ) and  $^*\text{OOH}$  ( $1042 \text{ cm}^{-1}$ ) relative to the applied potential were statistically shown in Fig. 5c. The vibration intensity of the  $^*\text{O}-\text{O}^*$  band increases rapidly as the OER potential exceeds 1.15 V. In contrast, the intensity of  $^*\text{OOH}$  for the Co-MOFs shows a relative slow enhancement after 1.25 V. This phenomenon suggests that the compression strain in BL-Co-MOFs accelerates the production of the active  $\text{CoOOH}$ -like phase for fast O—O coupling without the formation of the  $^*\text{OOH}$  species, thereby successfully regulating the inherent scaling relationship towards a fast OPM process.

### 3.5. Theory calculation on the structure model and electrocatalytic mechanism

The density functional theory (DFT) calculations were conducted to gain insights into the OER mechanism of BL-Co-MOFs. Considering that N, S, Mo element has no direct influence on the catalytic activity, and the catalytic active phase is the  $\text{CoOOH}$ -like phase generated by voltage driven. In the DFT simulations, we mainly considered two potential models, including conventional single-site ( $\text{CoOOH}$ ) and favorable dual-site models (dynamic-evolved  $\text{CoOOH}$  with shrinking Co—Co bonds) (Figure S29a). When considering the single site in  $\text{CoOOH}$  catalyst, the free energy of the rate-determining step (RDS) was relatively large as 1.60 eV as shown in Fig. 6a. However, following the introduction of compression strain, Fig. 6b shows the RDS for the dual-metal-site structural model in the dynamic-evolved  $\text{CoOOH}$  (BL-Co-MOFs) is the third proton–electron transfer steps of forming  $\text{O}^*$  from  $^*\text{OH}$ . As a result, the BL-Co-MOFs delivers a small free energy of 1.46 eV in the RDS and has optimal intermediate adsorption free energy. The calculated total density of states (TDOS) (Fig. 6c and Figure S29b) demonstrates that the compression strain in dynamic-evolved  $\text{CoOOH}$  exhibits a reduced band gap compared to  $\text{CoOOH}$ , indicating enhanced electrical conductivity of

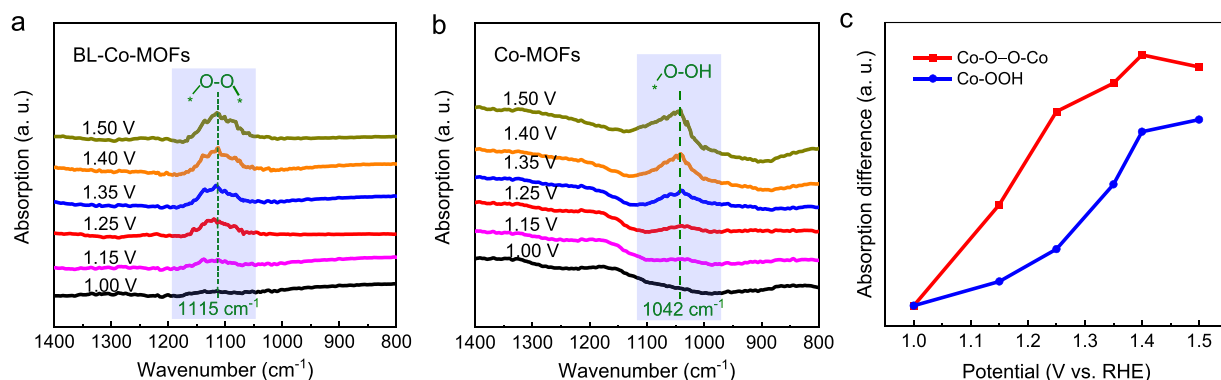


**Fig. 5.** *In situ* SR-FTIR spectra in the range of 800–1400  $\text{cm}^{-1}$  of (a) BL-Co-MOFs and (b) Co-MOFs (c) Intensity difference of the infrared signals at 1115  $\text{cm}^{-1}$  for BL-Co-MOFs and 1042  $\text{cm}^{-1}$  for Co-MOFs.

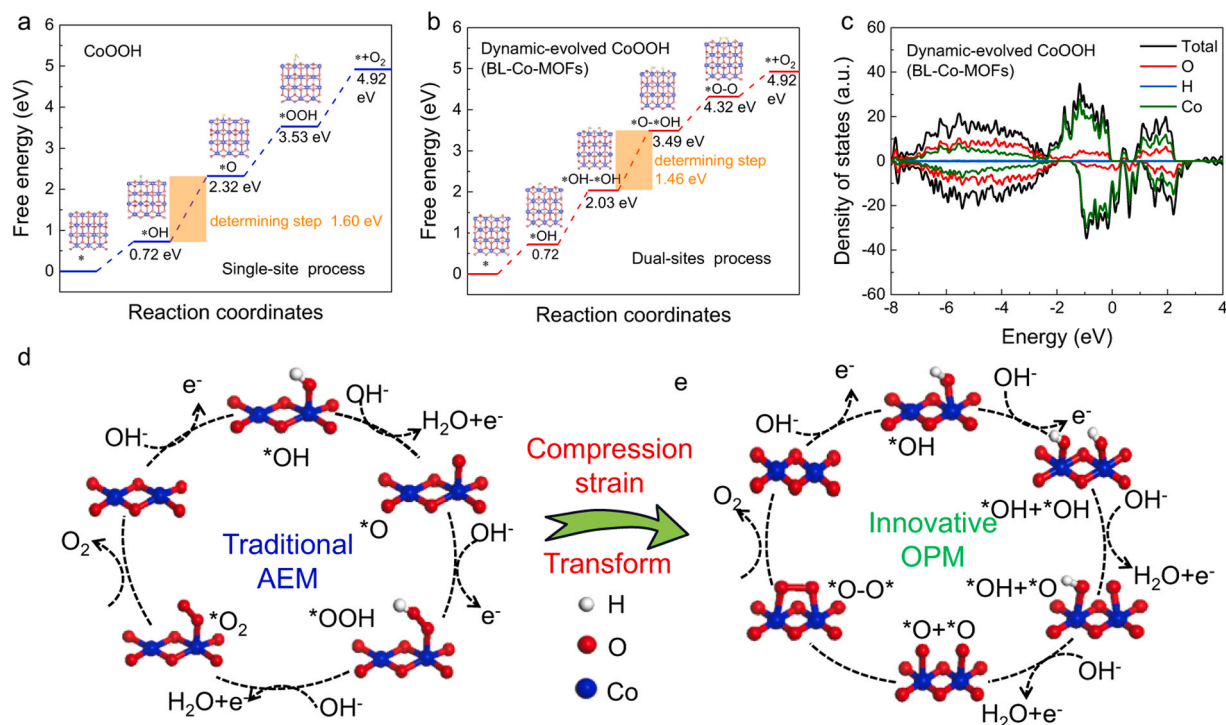


**Fig. 6.** Free energy diagram for OER on (a) CoOOH (blue line) and (b) dynamic-evolved CoOOH (red line). (c) The calculated projected density of states (PDOS) curves of dynamic-evolved CoOOH. (d) Schematic of the OER mechanism on the BL-Co-MOFs.

BL-Co-MOFs. Moreover, the differential charge density contour plot of BL-Co-MOFs clearly reveal a higher oxidation state after introducing compressive strain, further supporting its superior OER activity (Figure S29c). Consequently, the theoretical calculations corroborate the *in situ* XAFS and SRIR findings of the compressive strain in the potential-driven CoOOH-like phase, which is beneficial for direct O–O coupling over Co sites, thereby reducing limiting reaction barrier and following the OPM mechanism in BL-Co-MOFs during OER process.

The traditional AEM and innovative OPM reaction pathway mechanisms are summarized in Fig. 6d and Fig. 6e. For traditional AEM process, the  $\ast\text{OH}$  and  $\ast\text{OOH}$  intermediates are adsorbed on the single active sites by an end-on bonding state, which results in a slow kinetic process due to the difficulty of coupling the O–O bonds and deprotonation of  $\ast\text{OH}$  species. Delightfully, on the compression-strain BL-Co-MOFs, deprotonated  $\ast\text{OH}$  intermediates directly coupled to form  $\text{—O—O—}$  species over the adjacent Co atom pairs within the  $\text{Co—O—O—Co}$  structure, successfully bypassing the generation of the  $\ast\text{OOH}$  intermediates. Above all, these results show that the dynamically-evolved

CoOOH-like phase is real active sites during catalytic process. This CoOOH-like phase with compressive strain leads to direct O–O coupling over Co sites for a kinetic-fast OPM mechanism, successfully regulating the scaling relationship for the binding energies of multiple intermediates, and then significantly enhances the OER activity.

#### 4. Conclusion

In summary, we have successfully developed a bowl-like MOFs electrocatalyst (BL-Co-MOFs) with compression strain for efficient and stable OER performance. Mechanistic studies that employed *in situ* XAFS, Raman and SRIR spectroscopies reveal that dynamically-evolved CoOOH-like phase with contractive Co–Co distance can facilitate the direct O–O coupling over Co atom pairs ( $\text{Co—O—O—Co}$ ), which breaks the limit of the inherent linear scaling relationship and causes the OER on BL-Co-MOFs to follow a more kinetic-fast OPM pathway. As a result, the obtained BL-Co-MOFs catalyst delivers a high mass activity of 12516  $\text{A g}^{-1}$  at an overpotential of 275 mV (typically at a current

density of  $300 \text{ mA cm}^{-2}$ ), which is approximately 31 and 1526 times higher than those of Co-MOFs and commercial  $\text{RuO}_2$ , respectively. Interestingly, the BL-Co-MOFs shows stable water electrolysis for 80 h at a current density of  $100 \text{ mA cm}^{-2}$  with negligible performance degradation. This work provides a new strategy for constructing novel material structures and deepens the understanding of the dynamic mechanism of catalysts in promoting OER performance.

### CRediT authorship contribution statement

**Shuowen Bo:** Software, Investigation. **Jing Zhang:** Investigation, Data curation. **Meihuan Liu:** Writing – original draft, Methodology, Formal analysis. **Jun Pan:** Formal analysis, Data curation. **Hui Su:** Writing – review & editing, Supervision, Methodology, Investigation, Funding acquisition, Formal analysis, Conceptualization. **Qinghua Liu:** Project administration, Methodology, Data curation.

### Declaration of Competing Interest

The authors declare that they have no known competing financial interests or personal relationships that could have appeared to influence the work reported in this paper.

### Data Availability

Data will be made available on request.

### Acknowledgements

This work was supported by the National Key R&D Program of China (2022YFA1502903), the National Natural Science Foundation of China (12205300, 22241202, and U1932212), and the Natural Science Foundation of Anhui Province (2208085J01 and 2208085QA28).

### Appendix A. Supporting information

Supplementary data associated with this article can be found in the online version at [doi:10.1016/j.apcatb.2024.124114](https://doi.org/10.1016/j.apcatb.2024.124114).

### References

- N.T. Suen, S.F. Hung, Q. Quan, N. Zhang, Y.J. Xu, H.M. Chen, Electrocatalysis for the oxygen evolution reaction: recent development and future perspectives, *Chem. Soc. Rev.* 46 (2017) 337–365.
- L. Peng, N. Yang, Y. Yang, Q. Wang, X. Xie, D. Sun-Waterhouse, L. Shang, T. Zhang, G.I. Waterhouse, Atomic cation-vacancy engineering of NiFe-layered double hydroxides for improved activity and stability towards the oxygen evolution reaction, *Angew. Chem. Int. Ed.* 60 (2021) 24612–24619.
- Y. Zhao, X. Jia, G. Chen, L. Shang, G.I. Waterhouse, L.Z. Wu, C.H. Tung, D. O'Hare, T. Zhang, Ultrafine NiO nanosheets stabilized by  $\text{TiO}_2$  from monolayer NiTi-LDH precursors: an active water oxidation electrocatalyst, *J. Am. Chem. Soc.* 138 (2016) 6517–6524.
- C. Lin, J.L. Li, X. Li, S. Yang, W. Luo, Y. Zhang, S.H. Kim, D.H. Kim, S.S. Shinde, Y. F. Li, In-situ reconstructed Ru atom array on  $\alpha\text{-MnO}_2$  with enhanced performance for acidic water oxidation, *Nat. Catal.* 4 (2021) 1012–1023.
- W. Zhou, H. Su, W. Cheng, Y. Li, J. Jiang, M. Liu, F. Yu, W. Wang, S. Wei, Q. Liu, Regulating the scaling relationship for high catalytic kinetics and selectivity of the oxygen reduction reaction, *Nat. Commun.* 13 (2022) 6414.
- J. Song, C. Wei, Z.-F. Huang, C. Liu, L. Zeng, X. Wang, Z.J. Xu, A review on fundamentals for designing oxygen evolution electrocatalysts, *Chem. Soc. Rev.* 49 (2020) 2196–2214.
- R. Chen, Z. Wang, S. Chen, W. Wu, Y. Zhu, J. Zhong, N. Cheng, Activating lattice oxygen in spinel oxides via engineering octahedral sites for oxygen evolution, *ACS Energy Lett.* 8 (2023) 3504–3511.
- A. Bergmann, E. Martinez-Moreno, D. Teschner, P. Chernev, M. Gliech, J.F. De Araújo, T. Reier, H. Dau, P. Strasser, Reversible amorphization and the catalytically active state of crystalline  $\text{Co}_3\text{O}_4$  during oxygen evolution, *Nat. Commun.* 6 (2015) 8625.
- Z. Chen, L. Cai, X. Yang, C. Kronawitter, L. Guo, S. Shen, B.E. Koel, Reversible structural evolution of  $\text{NiCoO}_2\text{H}_2$  during the oxygen evolution reaction and identification of the catalytically active phase, *ACS Catal.* 8 (2018) 1238–1247.
- T. Reier, H.N. Nong, D. Teschner, R. Schlögl, P. Strasser, Electrocatalytic oxygen evolution reaction in acidic environments—reaction mechanisms and catalysts, *Adv. Energy Mater.* 7 (2017) 1601275.
- L. Xu, Q. Jiang, Z. Xiao, X. Li, J. Huo, S. Wang, L. Dai, Plasma-engraved  $\text{Co}_3\text{O}_4$  nanosheets with oxygen vacancies and high surface area for the oxygen evolution reaction, *Angew. Chem. Int. Ed.* 128 (2016) 5363–5367.
- Z. Shi, Y. Wang, J. Li, X. Wang, Y. Wang, Y. Li, W. Xu, Z. Jiang, C. Liu, W. Xing, Confined Ir single sites with triggered lattice oxygen redox: toward boosted and sustained water oxidation catalysis, *Joule* 5 (2021) 2164–2176.
- J. Hwang, R.R. Rao, L. Giordano, Y. Katayama, Y. Yu, Y. Shao-Horn, Perovskites in catalysis and electrocatalysis, *Science* 358 (2017) 751–756.
- E. Fabbri, T.J. Schmidt, Oxygen evolution reaction—the enigma in water electrolysis, *ACS Catal.* 8 (2018) 9765–9774.
- C. Roy, R.R. Rao, K.A. Stoerzinger, J. Hwang, J. Rossmeisl, I. Chorkendorff, Y. Shao-Horn, I.E. Stephens, Trends in activity and dissolution on  $\text{RuO}_2$  under oxygen evolution conditions: particles versus well-defined extended surfaces, *ACS Energy Lett.* 3 (2018) 2045–2051.
- N. Hodnik, P. Jovanović, A. Pavlišić, B. Jozinović, M. Zorko, M. Bele, V.S. Šelih, M. Šala, S. Hočevar, M. Gaberšek, New insights into corrosion of ruthenium and ruthenium oxide nanoparticles in acidic media, *J. Phys. Chem. C* 119 (2015) 10140–10147.
- C. Pasquini, I. Zaharieva, D. González-Flores, P. Chernev, M.R. Mohammadi, L. Guidoni, R.D. Smith, H. Dau, H/D isotope effects reveal factors controlling catalytic activity in Co-based oxides for water oxidation, *J. Am. Chem. Soc.* 141 (2019) 2938–2948.
- A. Bergmann, T.E. Jones, E. Martinez Moreno, D. Teschner, P. Chernev, M. Gliech, T. Reier, H. Dau, P. Strasser, Unified structural motifs of the catalytically active state of Co (oxyhydr) oxides during the electrochemical oxygen evolution reaction, *Nat. Catal.* 1 (2018) 711–719.
- A. Ali, F. Long, P.K. Shen, Innovative strategies for overall water splitting using nanostructured transition metal electrocatalysts, *Electrochem. Energy Rev.* 5 (2022).
- X.W. Lv, W.W. Tian, Z.Y. Yuan, Recent advances in high-efficiency electrocatalytic water splitting systems, *Electrochem. Energy Rev.* 6 (2023).
- S. Sha, R. Ge, Y. Li, J.M. Cairney, R. Zheng, S. Li, B. Liu, J. Zhang, W. Li, High-entropy catalysts for electrochemical water-electrolysis of hydrogen evolution and oxygen evolution reactions, *Front. Energy* (2023), <https://doi.org/10.1007/s11708-023-0892-6>.
- K. Wang, J. Huang, H. Chen, Y. Wang, W. Yan, X. Yuan, S. Song, J. Zhang, X. Sun, Recent progress in high entropy alloys forelectrocatalysts, *Electrochem. Energy Rev.* 5 (Suppl 1) (2022).
- R. Zhang, W. Liu, F.-M. Zhang, Z.-D. Yang, G. Zhang, X.C. Zeng, COF- $\text{C}_4\text{N}$  nanosheets with uniformly anchored single metal sites for electrocatalytic OER: from theoretical screening to target synthesis, *Appl. Catal. B: Environ.* 325 (2023) 122366.
- Z. Xiao, Y.C. Huang, C.L. Dong, C. Xie, Z. Liu, S. Du, W. Chen, D. Yan, L. Tao, Z. Shu, Operando identification of the dynamic behavior of oxygen vacancy-rich  $\text{Co}_3\text{O}_4$  for oxygen evolution reaction, *J. Am. Chem. Soc.* 142 (2020) 12087–12095.
- R. Gao, M. Deng, Q. Yan, Z. Fang, L. Li, H. Shen, Z. Chen, Structural variations of metal oxide-based electrocatalysts for oxygen evolution reaction, *Small Methods* 5 (2021) 2100834.
- T. Wu, S. Sun, J. Song, S. Xi, Y. Du, B. Chen, W.A. Sasangka, H. Liao, C.L. Gan, G. G. Scherer, Iron-facilitated dynamic active-site generation on spinel  $\text{CoAl}_2\text{O}_4$  with self-termination of surface reconstruction for water oxidation, *Nat. Catal.* 2 (2019) 763–772.
- X. Yuan, L. Zhang, L. Li, H. Dong, S. Chen, W. Zhu, C. Hu, W. Deng, Z.-J. Zhao, J. Gong, Ultrathin Pd–Au shells with controllable alloying degree on Pd nanocubes toward carbon dioxide reduction, *J. Am. Chem. Soc.* 141 (2019) 4791–4794.
- H. Su, W. Zhou, W. Zhou, Y. Li, L. Zheng, H. Zhang, M. Liu, X. Zhang, X. Sun, Y. Xu, In-situ spectroscopic observation of dynamic-coupling oxygen on atomically dispersed iridium electrocatalyst for acidic water oxidation, *Nat. Commun.* 12 (2021) 6118.
- H. Su, X. Zhao, W. Cheng, H. Zhang, Y. Li, W. Zhou, M. Liu, Q. Liu, Hetero-N-coordinated Co single sites with high turnover frequency for efficient electrocatalytic oxygen evolution in an acidic medium, *ACS Energy Lett.* 4 (2019) 1816–1822.
- Q. Wang, H. Liu, B. He, J. Qi, D. Wang, H. Xu, N. Zhang, J. Wang, Y. Chen, Z. Wang, Enhanced oxygen evolution reaction by stacking single-crystalline freestanding  $\text{SrRuO}_3$ , *Appl. Catal. B: Environ.* 317 (2022) 121781.
- M. Okamura, M. Kondo, R. Kuga, Y. Kurashige, T. Yanai, S. Hayami, V.K. Praneeth, M. Yoshida, K. Yoneda, S. Kawata, A pentanuclear iron catalyst designed for water oxidation, *Nature* 530 (2016) 465–468.
- M. Kōdera, Y. Kawahara, Y. Hitomi, T. Nomura, T. Ogura, Y. Kobayashi, Reversible O–O bond scission of peroxodiron (III) to high-spin oxodiron (IV) in dioxygen activation of a diiron center with a bis-tpa dinucleating ligand as a soluble methane monooxygenase model, *J. Am. Chem. Soc.* 134 (2012) 13236–13239.
- J. Pang, S. Yuan, D. Du, C. Lollar, L. Zhang, M. Wu, D. Yuan, H.C. Zhou, M. Hong, Flexible zirconium MOFs as bromine-nanocatalysts for bromination reactions under ambient conditions, *Angew. Chem. Int. Ed.* 129 (2017) 14814–14818.
- X. Xu, S. Chen, Y. Chen, H. Sun, L. Song, W. He, X. Wang, Polyoxometalate cluster-incorporated metal-organic framework hierarchical nanotubes, *Small* 12 (2016) 2982–2990.
- T. He, X. Xu, B. Ni, H. Lin, C. Li, W. Hu, X. Wang, Metal–organic framework based microcapsules, *Angew. Chem. Int. Ed.* 57 (2018) 10148–10152.

- [36] M. Zhang, D. Hu, Z. Xu, B. Liu, M. Boubeche, Z. Chen, Y. Wang, H. Luo, K. Yan, Facile synthesis of Ni-, Co-, Cu-metal organic frameworks electrocatalyst boosting for hydrogen evolution reaction, *J. Mater. Sci. Technol.* 72 (2021) 172–179.
- [37] P. Zhang, F. Qin, L. Zou, M. Wang, K. Zhang, Y. Lai, J. Li, Few-layered MoS<sub>2</sub>/C with expanding d-spacing as a high-performance anode for sodium-ion batteries, *Nanoscale* 9 (2017) 12189–12195.
- [38] W. Cheng, X. Zhao, H. Su, F. Tang, W. Che, H. Zhang, Q. Liu, Lattice-strained metal-organic-framework arrays for bifunctional oxygen electrocatalysis, *Nat. Energy* 4 (2019) 115–122.
- [39] M. Liu, Y. Li, Z. Qi, H. Su, W. Cheng, W. Zhou, H. Zhang, X. Sun, X. Zhang, Y. Xu, Self-nanocavity-confined halogen anions boosting the high selectivity of the two-electron oxygen reduction pathway over Ni-based MOFs, *J. Phys. Chem. Lett.* 12 (2021) 8706–8712.
- [40] X. Zhang, C. Yang, C. Gong, M. Liu, W. Zhou, H. Su, F. Yu, F. Hu, Q. Liu, S. Wei, Fast modulation of d-band holes quantity in the early reaction stages for boosting acidic oxygen evolution, *Angew. Chem. Int. Ed.* 62 (2023) e202308082.
- [41] Q. Ji, Y. Kong, H. Tan, H. Duan, N. Li, B. Tang, Y. Wang, S. Feng, L. Lv, C. Wang, Operando identification of active species and intermediates on sulfide interfaced by Fe<sub>3</sub>O<sub>4</sub> for ultrastable alkaline oxygen evolution at large current density, *ACS Catal.* 12 (2022) 4318–4326.
- [42] X. Li, Y. Tang, J. Zhu, H. Lv, L. Zhao, W. Wang, C. Zhi, H. Li, Boosting the cycling stability of aqueous flexible Zn batteries via F doping in nickel-cobalt carbonate hydroxide cathode, *Small* 16 (2020) 2001935.
- [43] Y. Zhu, W. Sun, W. Chen, T. Cao, Y. Xiong, J. Luo, J. Dong, L. Zheng, J. Zhang, X. Wang, Scale-up biomass pathway to cobalt single-site catalysts anchored on N-doped porous carbon nanobelt with ultrahigh surface area, *Adv. Funct. Mater.* 28 (2018) 1802167.
- [44] S. Geiger, O. Kasian, M. Ledendecker, E. Pizzutilo, A.M. Mingers, W.T. Fu, O. Diaz-Morales, Z. Li, T. Oellers, L. Fruchter, The stability number as a metric for electrocatalyst stability benchmarking, *Nat. Catal.* 1 (2018) 508–515.
- [45] H. Su, W. Zhou, H. Zhang, W. Zhou, X. Zhao, Y. Li, M. Liu, W. Cheng, Q. Liu, Dynamic evolution of solid–liquid electrochemical interfaces over single-atom active sites, *J. Am. Chem. Soc.* 142 (2020) 12306–12313.
- [46] Y. Hao, X. Cao, C. Lei, Z. Chen, X. Yang, M. Gong, Chemical oxygen species on electrocatalytic materials during oxygen evolution reaction, *Mater. Today Catal.* 2 (2023) 100012.
- [47] B.J. Trzeźniewski, O. Diaz-Morales, D.A. Vermaas, A. Longo, W. Bras, M.T. Koper, W.A. Smith, In situ observation of active oxygen species in Fe-containing Ni-based oxygen evolution catalysts: the effect of pH on electrochemical activity, *J. Am. Chem. Soc.* 137 (2015) 15112–15121.
- [48] H.Y. Wang, S.F. Hung, Y.Y. Hsu, L. Zhang, J. Miao, T.S. Chan, Q. Xiong, B. Liu, In situ spectroscopic identification of  $\mu$ -OO bridging on spinel Co<sub>3</sub>O<sub>4</sub> water oxidation electrocatalyst, *J. Phys. Chem. Lett.* 7 (2016) 4847–4853.
- [49] B.N. Zope, D.D. Hibbitts, M. Neurock, R.J. Davis, Reactivity of the gold/water interface during selective oxidation catalysis, *Science* 330 (2010) 74–78.
- [50] A. Yao-Lin, Z.Y. Du, H.J. Ze, X.T. Wang, Y. Zhang, H. Zhang, Q.N. Zheng, J. C. Dong, J.H. Tian, J.F. Li, Understanding the molecular mechanism of oxygen reduction reaction using in-situ raman spectroscopy, *Curr. Opin. Electrochem.* (2023) 101381.
- [51] W. Cheng, H. Su, Q. Liu, Tracking the oxygen dynamics of solid–liquid electrochemical interfaces by correlative in situ synchrotron spectroscopies, *Acc. Chem. Res.* 55 (2022) 1949–1959.
- [52] B. Wang, K. Zhao, Z. Yu, C. Sun, Z. Wang, N. Feng, L. Mai, Y. Wang, Y. Xia, In situ structural evolution of the multi-site alloy electrocatalyst to manipulate the intermediate for enhanced water oxidation reaction, *Energy Environ. Sci.* 13 (2020) 2200–2208.
- [53] R.R. Rao, M.J. Kolb, L. Giordano, A.F. Pedersen, Y. Katayama, J. Hwang, A. Mehta, H. You, J.R. Langer, H. Zhou, Operando identification of site-dependent water oxidation activity on ruthenium dioxide single-crystal surfaces, *Nat. Catal.* 3 (2020) 516–525.
- [54] M. Liu, H. Su, W. Cheng, F. Yu, Y. Li, W. Zhou, H. Zhang, X. Sun, X. Zhang, S. Wei, Synergetic dual-ion centers boosting metal organic framework alloy catalysts toward efficient two electron oxygen reduction, *Small* 18 (2022) 2202248.